(Received 20 December 2025, Accepted 25 February 2026, Scheduled 15 March 2026)

12-Port SRR Loaded Flower-Shaped UWB MIMO Antenna System for 5G Smartphones

Diksha Thakur[1] and Naveen Jaglan[2,*]

[1] *Department of Electronics and Communication Engineering, Jaypee University of Information Technology, Waknaghat, Solan, Himachal Pradesh, India*
[2] *Centre of Excellence in 5G Technology & IoT, Department of Electronics and Communication Engineering, Netaji Subhas University of Technology, Sector-3, Dwarka, New Delhi, India*

ABSTRACT: This article presents a 12-element multiple-input multiple-output (MIMO) antenna system for fifth-generation mobile phones. To improve isolation, split-ring resonators are positioned adjacent to the radiating elements in the proposed design, which features a flower-shaped antenna radiator etched along the side frames of the device. The antenna system provides an isolation of over 15 dB between the elements with a wide operational band of 3.0–7.5 GHz. Simulations and experiments demonstrate that sublime presentations have an overall efficiency of 58%–78% across the operational band and an ECC of less than 0.05. Additionally, the impact of user's hand grip, plastic frame, and battery integration is analyzed. The robustness of the proposed design was confirmed by the alignment between the simulated and measured results.

1. INTRODUCTION

The rapid advancement of wireless communication systems over the past few years, driven by fifth-generation (5G) networks, has imposed stringent requirements on antenna systems in modern mobile terminals. In particular, these advanced antenna systems must support wideband operation, high data rates, and low latency, while providing reliable connectivity despite limited space. These requirements led researchers to adopt MIMO technology to meet these needs [1, 2]. Significant research has been carried out to address these challenges. A 10-element multiband MIMO array that achieves wide coverage across 3.3–3.8 GHz and 5.0–5.9 GHz for 5G smartphones is presented [3]. In [4], the authors designed a wideband decoupled 8-element array, focusing on isolation enhancement where F-shaped radiators are fed by L-shaped structures with a T-shaped decoupling design, while a coupled-loop 8-element antenna is used to accomplish a 3.3–5.8 GHz frequency range for a mobile phone [5]. An 8-element monopole MIMO antenna with a printed monopole on the side frame and a simple feed is integrated. The antenna is arranged so as to reduce coupling and to achieve a working band of 3.4–3.6 GHz [6]. An Inverted-F Antenna (IFA) mode with slots features a rectangular slot on the ground plane with a side-edge etched gap. Wideband functionality is achieved by adjusting and merging the two modes using a tuning stub and a meandering impedance transformer [7]. Orthogonal placement and decoupling structures are used for an 8-port MIMO antenna to suppress mutual coupling, operating at the 3.3–6 GHz range [8]. Triple-band operation covering 3.3–3.6 GHz, 4.8–5 GHz, and 5.1–5.3 GHz is achieved using a multi-slot antenna with ground modification. It consists of eight compact elements arranged symmetrically for MIMO applications, while a dual-band 8×8 MIMO array covering 3.3–3.6 GHz and 4.8–5 GHz is achieved using a U-shaped antenna with an L-shaped slot at the ground plane [9, 10].

Closely packed four-element MIMO antennas for 5G smartphones are introduced, achieving compact placement by improving element orientation and ground modification [11]. The design achieved sufficient isolation and efficiency. This concept is extended in [12] by introducing multi-slot decoupling for an eight-element MIMO array. The slots introduced in the ground plane helped reduce mutual coupling and can be used in sub-6 GHz smartphone applications. A miniaturized MIMO antenna is proposed that achieves stable impedance matching and isolation across its operating band by reducing its size and utilizing limited smartphone space [13]. Careful placement of antenna elements within the confined space is used to achieve the performance parameters [14], while [15] utilizes a wideband MIMO antenna with orthogonal-mode dual-antenna pairs. T- and C-shaped slots are used, while an H-shaped slot is used between two antenna elements to mitigate coupling [16]. An 18-element massive MIMO antenna system emphasizes diversity performance and spatial multiplexing; however, it increased design complexity and space requirements [17]. Three differently-shaped radiators are combined with a defective ground structure (DGS) having T-shaped slots operating at 3.5 GHz, 4.9 GHz, and 5.7 GHz to enhance isolation [18], while [19] consists of eight elements having a rectangular slot with L-shaped feed with an H-shaped DGS operating at a frequency range of 3.4 to 6.5 GHz. Slots are etched on the patch to create multiple resonances, enabling wideband operation (3.15–5.55 GHz) and LTE applications. They also improve impedance matching across the desired bands, achieving a max-

* Corresponding author: Naveen Jaglan (naveenjaglan1@gmail.com).

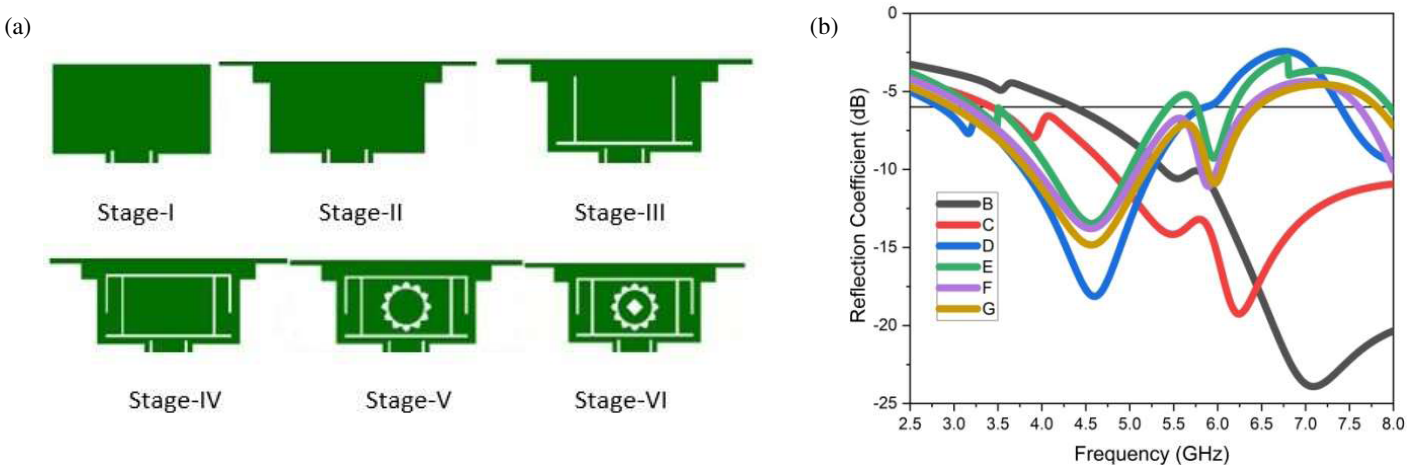

FIGURE 1. (a) Systematic designing stages of a single proposed antenna. (b) Reflection coefficient for the design stages.

imum radiation efficiency of 79.6% [20]. Slots and metal with shorting pins are combined to form a decoupling structure to reduce mutual coupling. A metasurface is applied to the substrate to suppress unwanted coupling and to operate effectively between 3.3 and 3.87 GHz. 5G categorization is based on various frequency bands, which have been adopted worldwide for communication [21].

A 4×4 flower-shaped ultra-wideband (UWB) MIMO antenna is designed without using decoupling structures [23], helping in optimizing current distribution and reducing mutual coupling among elements. A compact 4-port MIMO antenna employs decoupling structures on the top and bottom sides of the substrate, with slots in the ground plane, to achieve good isolation between antennas [24]. A two-element, flower-shaped antenna incorporating complementary split-ring resonators (CSRRs) is designed for an ultra-wideband MIMO antenna with dual notching, thereby improving isolation [25]. In [26], the implementation of CSRRs in antenna design yields a compact size, improved gain, and radiation efficiency by quelling surface currents. Further, decreasing mutual coupling and tuning resonance frequencies assist their integration with MIMO antenna systems.

The role of metamaterials in miniaturization, gain enhancement, bandwidth improvement, and isolation is discussed, with emphasis on various methods and integration techniques. It emphasizes the potential of metasurfaces to control EM waves for antenna functionalities [27]. A 2-element circular MIMO patch antenna is designed with a metamaterial to improve antenna performance by reducing mutual coupling. The antenna is designed for 28 GHz. In [28], a metamaterial is placed between the antenna elements, whereas in [22], a quad-port MIMO antenna with a flower pattern is designed, incorporating a bandpass filter to suppress unwanted signals and improve antenna performance. Despite these advances, these strategies have not yet been applied to side-frame smartphone antennas. The combination of them remains unexplored. Etching antenna elements into the side frame reduces space on the main printed circuit board (PCB), enabling compact antenna designs with greater separation, thereby improving isolation and efficiency.

In this study, an integrated side-frame antenna for 5G smartphones operating in the UWB is proposed. Therefore, this design provides good isolation with broad bandwidth, accommodating the spatial constraints of modern devices. Furthermore, additional optimization was realized by adding slots to the side frame of the design for compact systems, thereby merging slot structures and metamaterial design. Therefore, the antenna design operates between 3.0 and 7.5 GHz, achieving up to 78% efficiency and more than 15 dB of isolation. The remainder of this paper is organized as follows. Section 2 presents the proposed UWB MIMO antenna design. In Section 3, the results of simulations and measurements are evaluated. In Section 4, the proposed design is compared to other similar antenna systems in the literature. Section 5 presents a practical submission, including the user grip, battery placement, and plastic frame material. Finally, Section 6 draws a conclusion of the paper.

2. SUGGESTED UWB MIMO ANTENNA SYSTEM DESIGN

Achieving such a wide impedance bandwidth requires comprehensive and well-documented design parameters, including the precise dimensions of the radiating element and slots, substrate material properties (dielectric constant, loss tangent, and thickness), ground plane configuration, feeding technique, and mutual coupling mitigation strategy. The bandwidth performance is highly sensitive to these parameters, and even minor dimensional variations can significantly shift the resonant frequencies and degrade impedance matching. Figure 1(a) illustrates the step-by-step evolution of the proposed antenna structure from a simple patch configuration (Stage I) to the final optimized geometry (Stage VI), where each modification systematically alters the operating frequency response. In Stage III, the introduction of slots increases the effective electrical length of the current path, thereby improving impedance matching without increasing the physical size of the antenna. This modification results in an operating band of 3.43–5.5 GHz. In Stage IV, an additional slot is introduced in the upper region of the radiating element, producing dual operating bands of 3.5–5.5 GHz and 5.75–6 GHz. Stage V incorporates a circular ring-slot structure

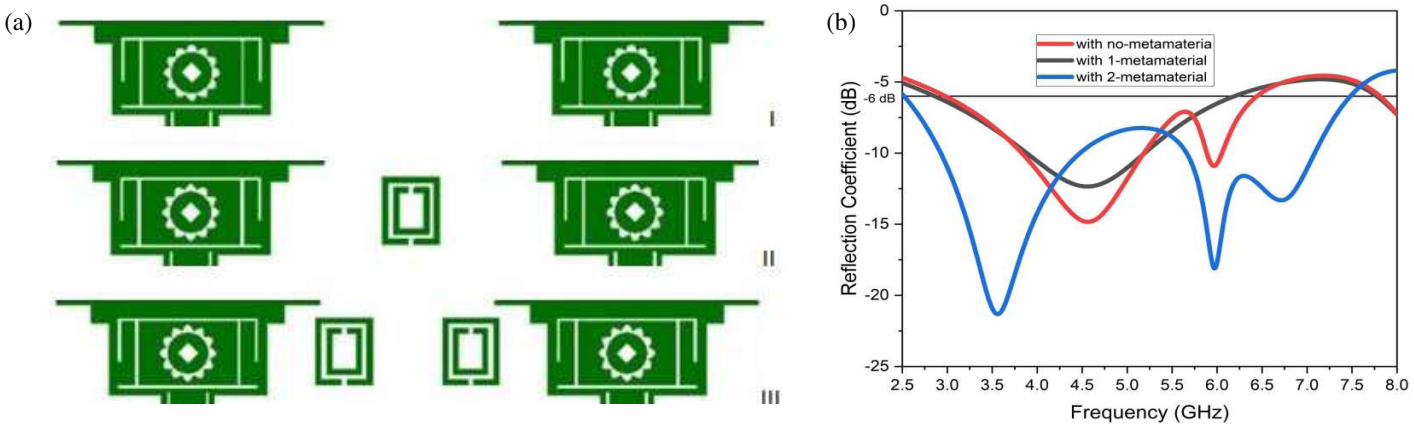

FIGURE 2. (a) Systematic for metamaterial loading design. (b) Reflection coefficient for the same.

with a flower-like configuration, which facilitates the excitation of multiple closely spaced resonant modes and extends the impedance bandwidth to 3.3–6.2 GHz. Finally, in Stage VI, a diamond-shaped slot is introduced to further refine resonance coupling, resulting in an enhanced 6 dB impedance bandwidth of 3.2–6.3 GHz.

Figure 1(b) presents the simulated reflection coefficient (S_{11}) as a function of frequency for all design stages, demonstrating the progressive bandwidth enhancement achieved through each structural modification. The stages are labeled from Stage I to Stage VI in Figure 1(a) and are correspondingly denoted as B to G in Figure 1(b), where B represents Stage I; C represents Stage II; D represents Stage III; E represents Stage IV; F represents Stage V; and G represents Stage VI.

Figure 2(a) depicts the effect of metamaterial loading on the antenna structure design, and its reflection coefficient is shown in Figure 2(b). Mutual coupling is minimized through the integration of SRR-type metamaterial structures between antenna elements. The antenna is designed by integrating metamaterial unit cells in 3 distinct configurations to modify its electromagnetic behavior. These unit cells increase the effective permittivity and permeability, thereby altering the current distribution in the design. Figure 2(b) compares the reflection coefficient for these three designs, that is, without metamaterial and with single and double metamaterial loading. The metamaterial-loaded design exhibits deeper resonance dips and additional resonant bands. It shows improved impedance matching and an enhanced band. Overall, the incorporation of metamaterials significantly improves bandwidth and antenna performance.

The proposed MIMO antenna system comprises 12 antenna elements, labelled Ant1–Ant12, as depicted in Figure 3(a). This antenna is designed for ultra-wideband 5G smartphones, with a footprint of 150 mm × 75 mm × 0.8 mm. The circuit board and side frames are built using an FR4 substrate, which has a dielectric constant (ε_r) of 4.4 and a loss tangent ($\tan\delta$) of 0.02. In the proposed layout, antenna elements are symmetrically placed along the right (dexter) and left (sinister) sides of the system circuit board. Each of the elements is 15 mm × 7 mm in dimensions (length × height). Figure 3(b) illustrates the design of one element of an antenna containing split ring resonators (SRRs) for further improvement in performance.

The detailed geometrical dimensions of the proposed antenna are provided to ensure reproducibility of the design. The radiating element dimensions shown in Figure 3(c) are defined as follows: $f = 1$ mm, $w = 4.1$ mm, $g = 0.7$ mm, $h = 0.9$ mm, $e = 8$ mm, $a = 3.6$ mm, $b = 2.3$ mm, $c = 1$ mm, and $d = 2$ mm. The flower-shaped structure illustrated in Figure 3(e) consists of $C_R = 1.16$ mm, $P_R = 1.64$ mm, and $P_1 = 0.49$ mm. The flower geometry is formed by intersecting two circles of radius 0.6 mm to create a single petal, and twelve identical petals are symmetrically arranged to generate the complete flower structure. The diamond-shaped element shown in Figure 3(e) has dimensions $D_R = 0.6$ mm, $j = 0.55$ mm, and $i = 0.6$ mm. Furthermore, the SRR dimensions depicted in Figure 3(d) are specified as $k = 3.2$ mm, $l = 3.8$ mm, $m = 0.3$ mm, $r = 0.3$ mm, $n = 2$ mm, $o = 1.4$ mm, $p = 0.3$ mm, $q = 1.15$ mm, $s = 0.3$ mm, and $t = 2$ mm. These dimensions correspond to the optimized configuration used to achieve the reported operating bandwidth.

Decoupling structures increases the current distribution of parasitic elements. The current distribution around the decoupling design was investigated for three configurations: without a decoupling element, with one decoupling element, and with two decoupling elements. As shown in Figure 4(a), no separating designs are positioned between two radiating elements; a strong distribution of current is induced by mutual coupling effects on the neighboring antenna elements. In Figure 4(b), one SRR element is used as a decoupling element; the current induces mutual inductance effects on the neighboring antenna elements. This can be regarded as a partial mitigation of the coupling effects. Finally, Figure 4(c) presents two decoupling structures implemented between the radiating antennas, resulting in a current distribution with a less significant effect on the neighboring radiating elements; thus, mutual coupling is effectively suppressed. In Figures 4(a), 4(b), and 4(c), the current distribution results, only one port is excited at a time, with all other ports terminated with 50 Ω loads.

3. RESULTS AND DISCUSSION

The simulation and modelling of this suggested design were conducted using ANSYS HFSS v22. A prototype was fabri-

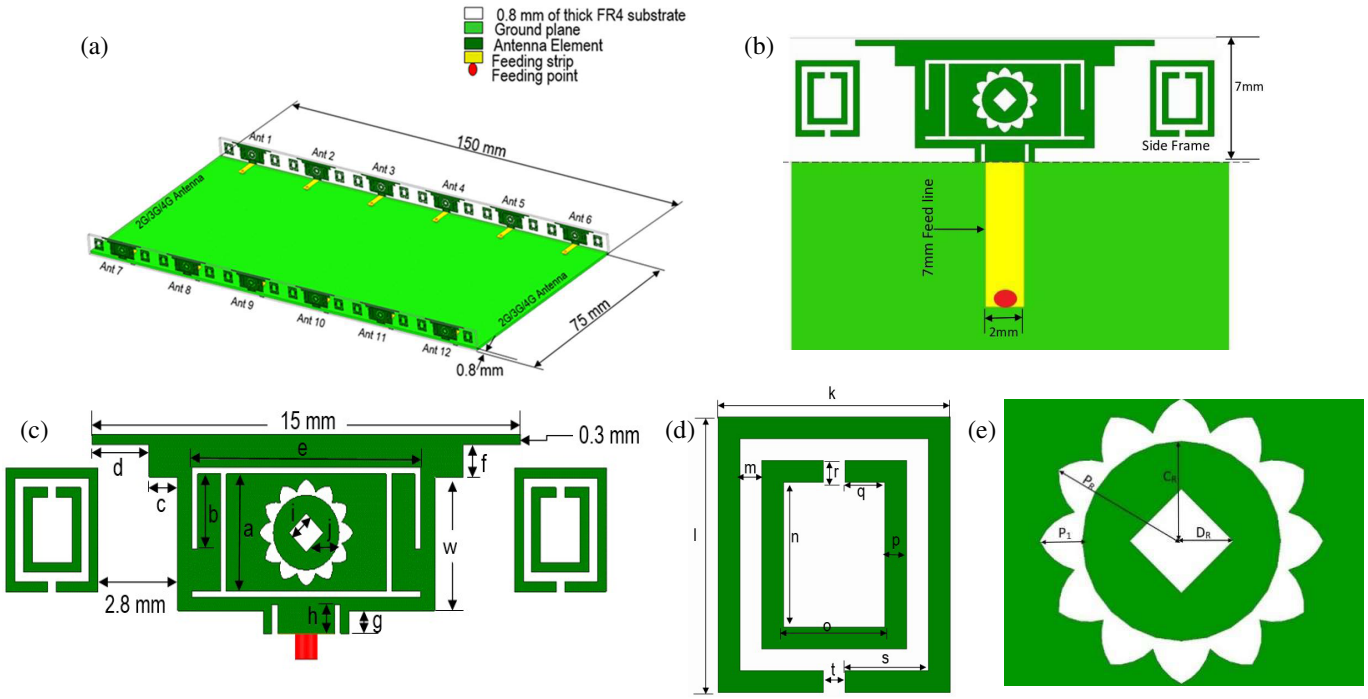

FIGURE 3. Schematic of suggested UWB MIMO antenna system: (a) General layout of the PCB. (b) Side-mounted view showing the design. (c) Single antenna element dimensions. (d) SRR dimensions. (e) Inner dimension of design.

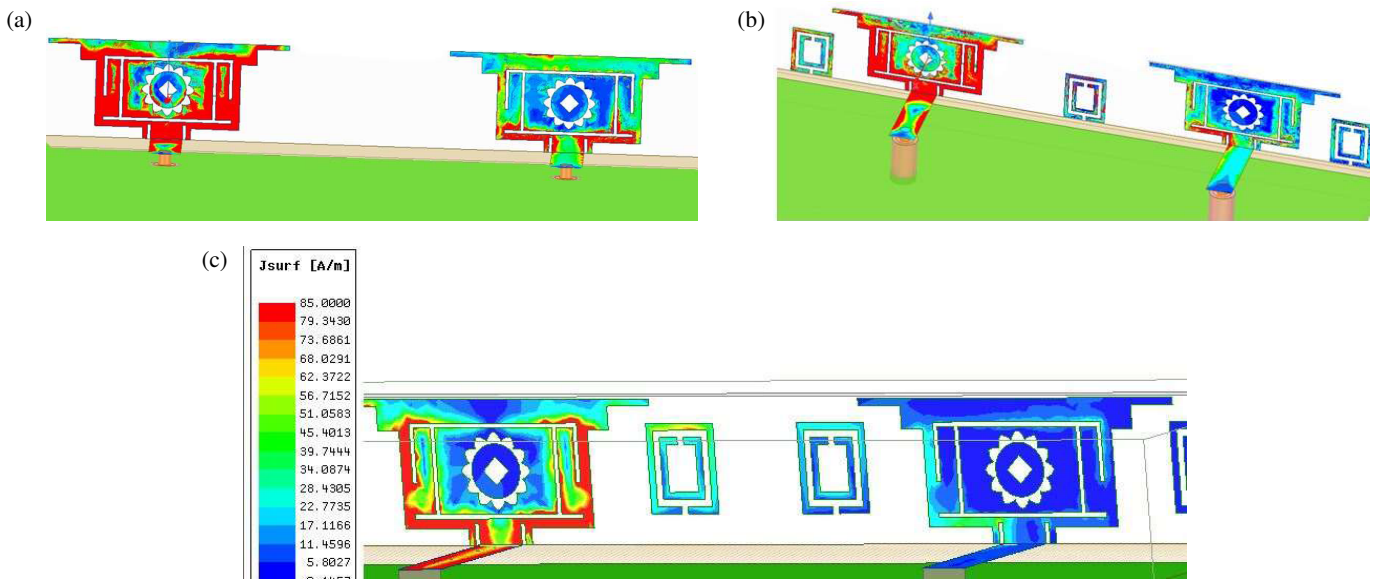

FIGURE 4. Current distribution within Ant1 and Ant2: (a) Without SRR structure, (b) One SRR structure, (c) Two SRR structures, placed among the antenna elements.

cated to evaluate the simulation results, as shown in Figure 5. In this model, a 50-ohm SMA connector was employed to supply power to all 12 ports. The layout of the proposed antenna system is illustrated in Figure 5. The performance and effectiveness of the prototype were tested in a microwave-shielded anechoic chamber to ensure precise and unobstructed results.

3.1. S-Parameters, Efficiency, and Radiation Patterns

Figure 6(a) depicts simulated reflection coefficients ($S_{i,i}$: $S_{1,1}S_{2,2}$, …., $S_{12,12}$) for the suggested 12-element MIMO antenna array; on the other hand, Figure 6(b) shows its measured results. They both depict that the proposed antenna elements exhibit a similar pattern of S-parameters, thus depicting that both Figures 6(a) and 6(b) are in good symmetry. Using a -6 dB reflection coefficient as the reference, the antenna satisfies UWB operation across the 3–7.5 GHz frequency range. There are minor frequency shifts and slight degradation in matching at the upper band, owing to fabrication, connector, or soldering effects; however, the operating bandwidth remains below -6 dB and is in agreement. Figures 7(a) and 7(b)

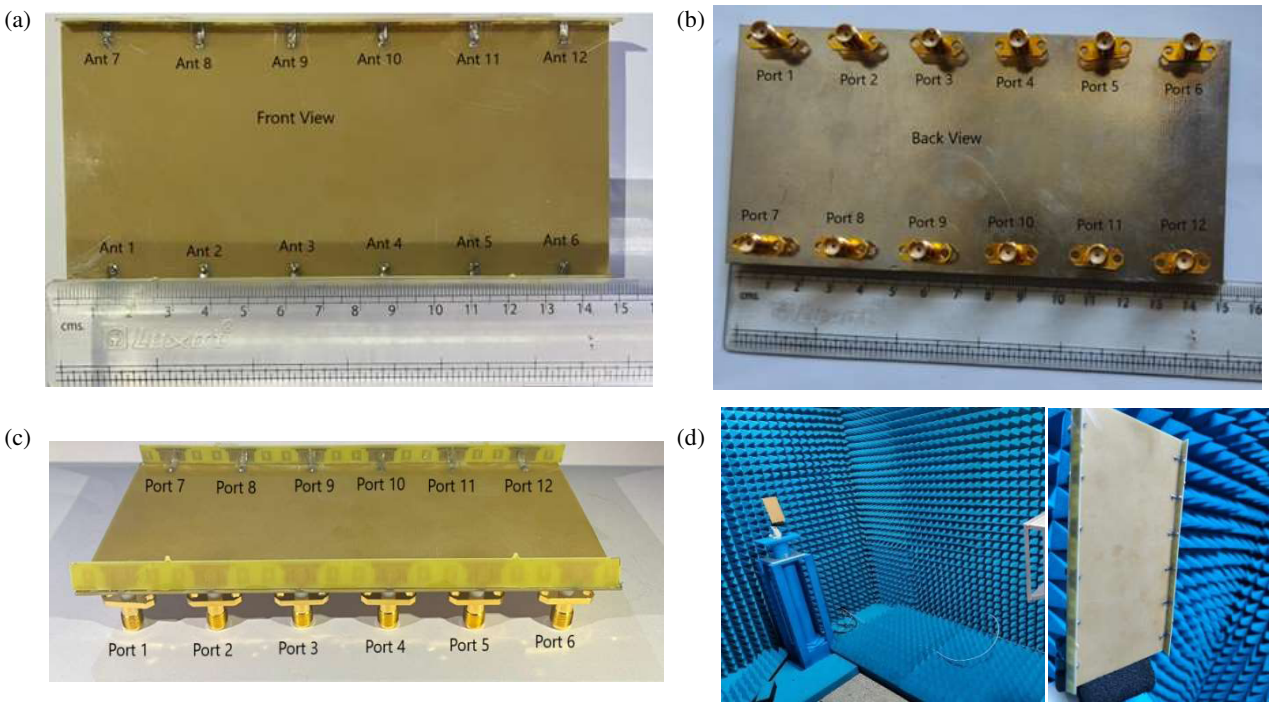

FIGURE 5. Fabricated design paradigm: (a) Apex vision, (b) Rear vision, (c) Side vision, (d) Measurement setup inside the anechoic testing chamber.

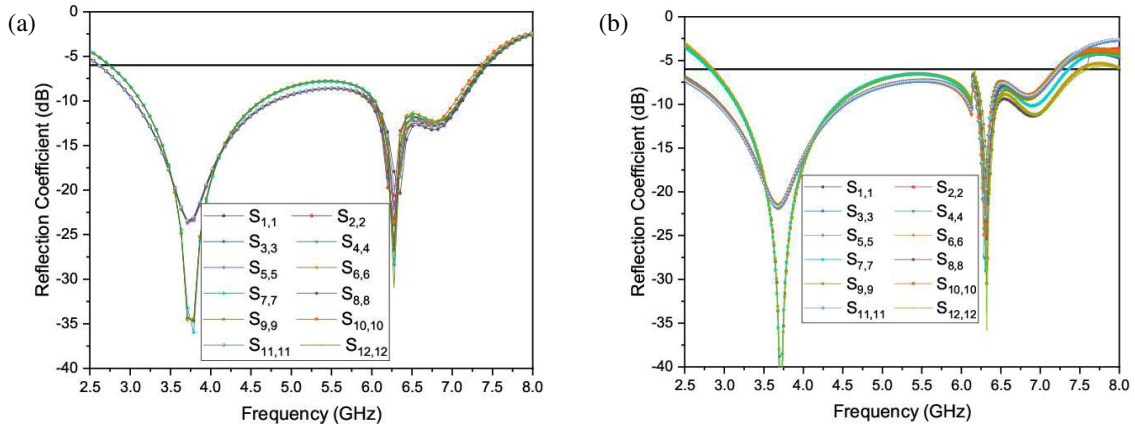

FIGURE 6. Recommended antenna design's Reflection Coefficients (a) Simulated, (b) Measured.

indicate simulated and measured transmission coefficients ($S_{i,j}$: $S_{1,2}$, $S_{2,3}$, …., $S_{11,12}$). Effective isolation is shown in Figure 7, which maintains a transmission coefficient below -15 dB across the operating band in both simulated and measured results. Minor discrepancies are expected from antennas' resonant behavior, while the overall trend remains the same.

Figure 8(a) illustrates the efficacy of the suggested MIMO antenna, showing efficiency values ranging from 58% to 78% across the overall frequency range. The highest efficiency (78%) occurs at the lower end (3 GHz), whereas efficiency ($\sim$58%) decreases toward the upper frequency band (7.5 GHz) for the proposed antenna. The graph also shows the antenna without metamaterials and with a single metamaterial, with efficiency values lower than those of the antenna with two metamaterial elements.

The degradation at higher bands can be attributed to conductor loss and increased dielectric losses within the antenna designs, along with impedance mismatch as the frequency moves away from the main resonant modes. The peak gain of the recommended antenna system is shown in Figure 8(b), with radiation efficiency for a single antenna element presented for three cases: no metamaterial between antennas, one metamaterial element placed between antennas, and two metamaterial elements placed among the antenna elements. Figure 9 presents the measured and simulated radiation patterns of Antennas 1–6 in the xy-plane.

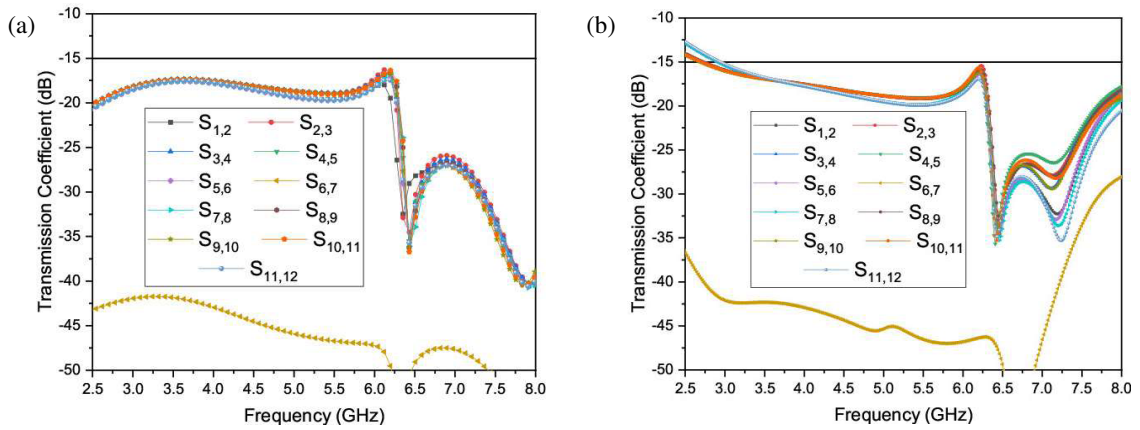

FIGURE 7. Recommended antenna's mutual coupling plots: (a) simulated transmission coefficient and (b) measured transmission coefficient.

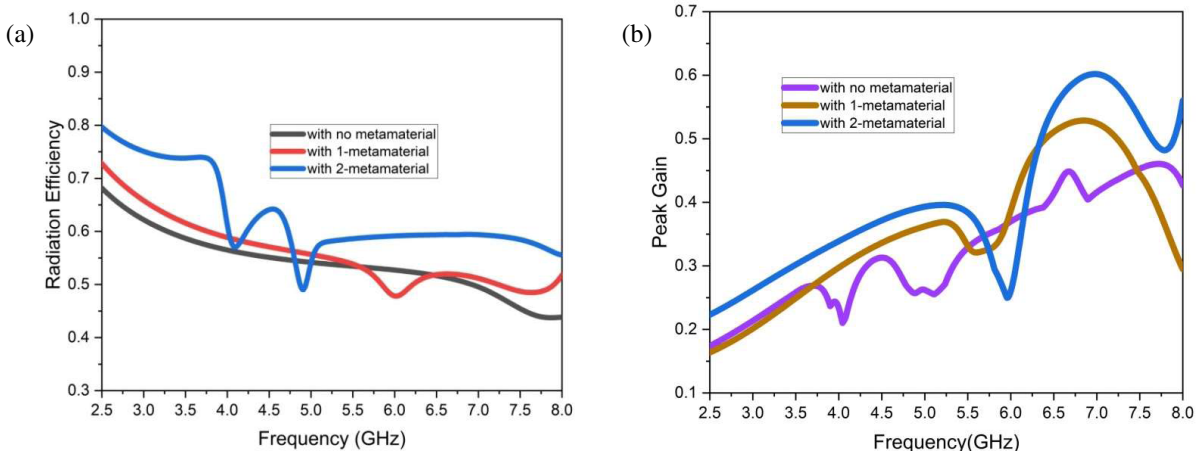

FIGURE 8. (a) Antenna efficiency results. (b) Peak gain results, for the proposed antenna with three different scenarios.

3.2. MIMO Performance

In a MIMO antenna system, the relationship between the near-field patterns of two radiating elements is measured using the Envelope Correlation Coefficient (ECC). ECC is an essential parameter to be considered when the diversity gain of a MIMO system is measured. In 5G MIMO systems, a high diversity performance is achieved when the ECC values remain below 0.5. As the antenna elements in this design are homogeneous, the results for some of the antenna elements are presented. The ECC between Ant i and Ant j (ρ_{ij}) was computed by applying the following formula for far-field radiation patterns [17]:

$$\rho_{ij} = \left| \frac{\int_0^{2\pi}\int_0^{\pi}\left(XPR\cdot E_{\theta i}\cdot E^*_{\theta j}\cdot P_\theta + XPR\cdot E_{\phi i}\cdot E^*_{\phi j}\cdot P_\phi\right) Sin(\theta)d\theta d\phi}{\sqrt{\prod_{\kappa=i,j}\int_0^{2\pi}\int_0^{\pi}\left(XPR\cdot E_{\theta k}\cdot E^*_{\theta k}\cdot P_\theta + XPR\cdot E_{\phi k}\cdot E^*_{\phi k}\cdot P_\phi\right) Sin(\theta)d\theta d\phi}} \right|^2 \quad (1)$$

Here, $E_{\theta i}$, $E_{\theta j}$, $E_{\phi i}$, $E_{\phi j}$ represent the far-field components of the antenna elements, while the cross-polarization ratio (XPR) refers to the ratio of the vertically and horizontally polarized components. Subscripts E_θ and E_ϕ indicate azimuth and elevation polarizations, respectively. P_θ and P_ϕ indicate the angular power spectra of propagation environment. The ECC values evaluated for various antenna elements are presented in Figure 10. The results show that the simulated and measured ECC values remain below 0.05 across the entire operational bandwidth, indicating excellent diversity performance. The antenna design is symmetric in nature and exhibits similar characteristics. The omission of certain antennas does not imply that they have different ECC values. Including all 12 elements would create clutter; only a subset of these antenna elements is shown to avoid confusion. Figure 10(a) shows ECC simulated for a few antenna element combinations, while Figure 10(b) shows measured results for the same antenna combination for the suggested antenna. The y-axis of the measured results is marked in increments of 0.005 to improve clarity. The difference between Figures 10(a) and 10(b) can be mainly attributed to some fabrication tolerances, connectors, cable effect, or materials that cannot be fully captured in simulations. Small physical changes also significantly impact ECC, making it more sensitive than S-parameters.

Channel capacity symbolizes the data proportion that can be channelized without errors, while the channel capacity loss (CCL) quantifies the percentage of this capacity that is lost due to errors.

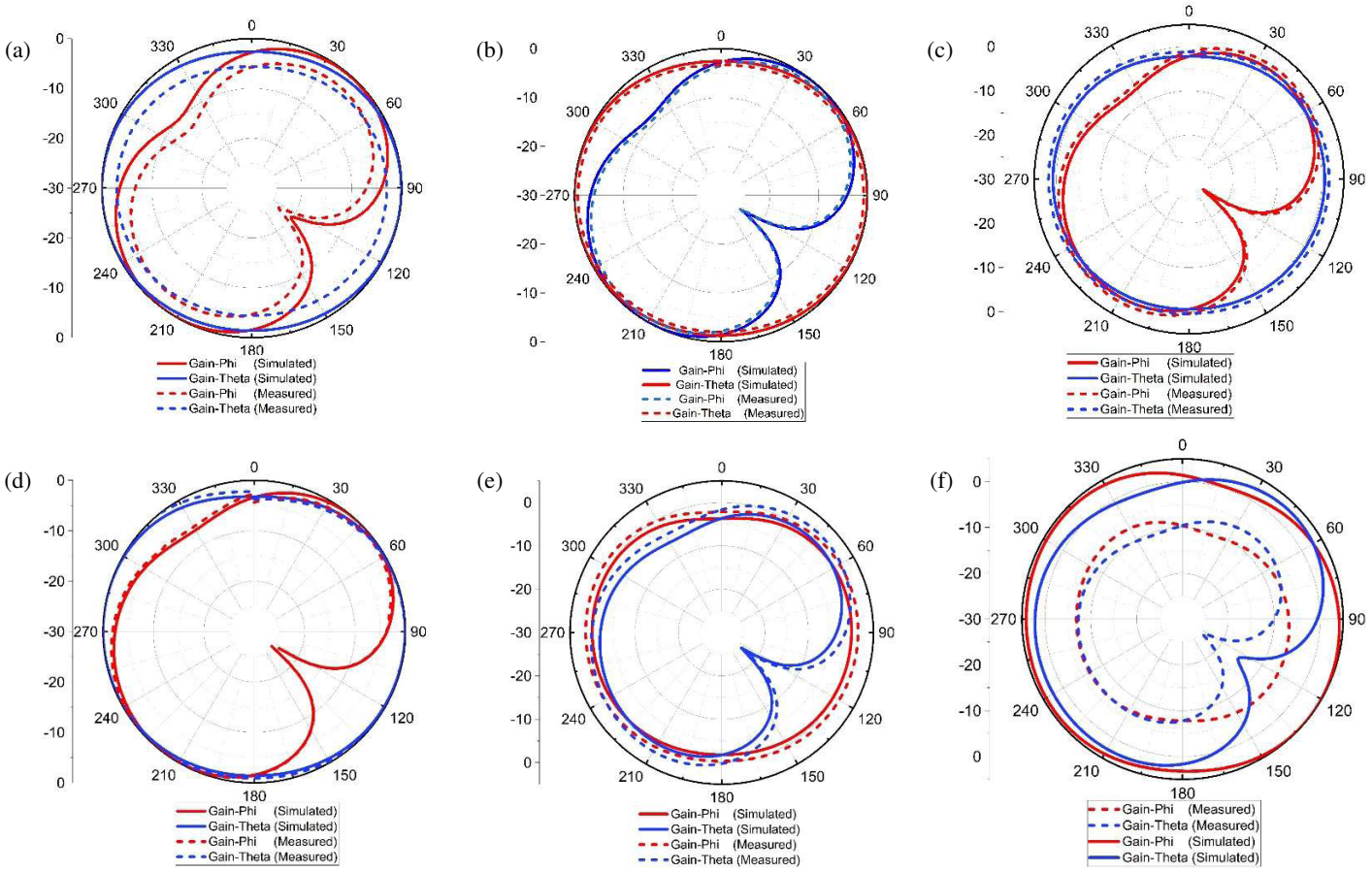

FIGURE 9. Radiation pattern of the proposed antenna at 7 GHz. (a) Ant1. (b) Ant2. (c) Ant3. (d) Ant4. (e) Ant5. (f) Ant6.

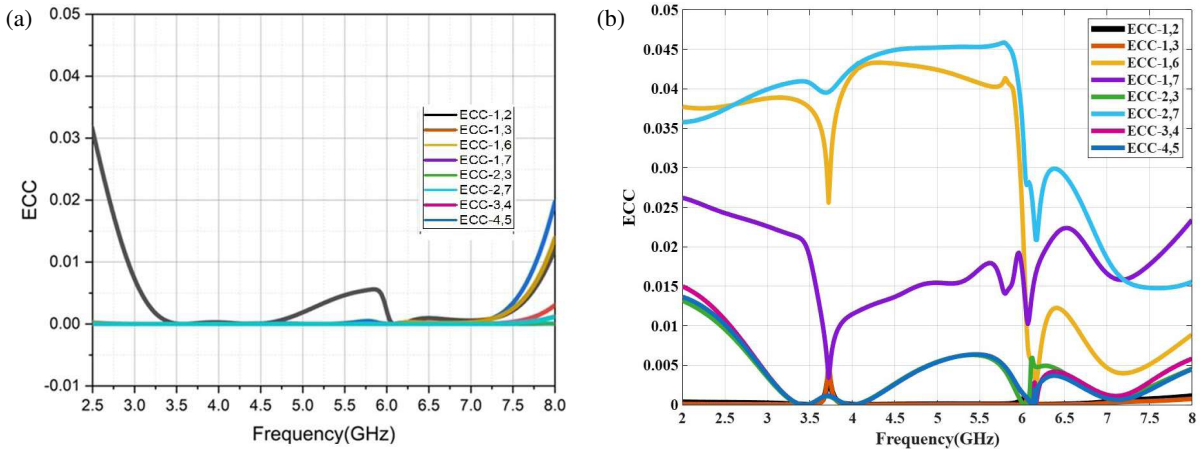

FIGURE 10. Variations in ECC among different antenna pairs. (a) Simulated ECC. (b) Measured ECC.

In the CCL formulation, the determinant operator is denoted by det(b), where b represents the two-port antenna correlation matrix. The self- and cross-correlation terms between antenna elements i and j are given by the matrix elements σ_{ii}, σ_{jj}, and $\sigma_{ij} = \sigma_{ji}^*$, respectively. In the functioning band (3.0 GHz–7.5 GHz), the CCL value remains below 0.4 bit/sec/Hz. The calculated CCL of the prototype is shown in Figure 11(a). The following equations [18] were used to calculate CCL values:

$$CCL = -\log_2 \det(b) \tag{2}$$

Here,

$$b = \begin{bmatrix} \sigma_{ii} & \sigma_{ij} \\ \sigma_{ji} & \sigma_{jj} \end{bmatrix} \tag{3}$$

Figure 11(b) shows the mean effective gain (MEG). The values of MEG1, MEG2, and MEG3 were very similar, with a difference of less than 3 dB. The equality condition for the two antenna elements was met, as the proportions of MEG1/MEG2 and MEG1/MEG3 were nearly 1.

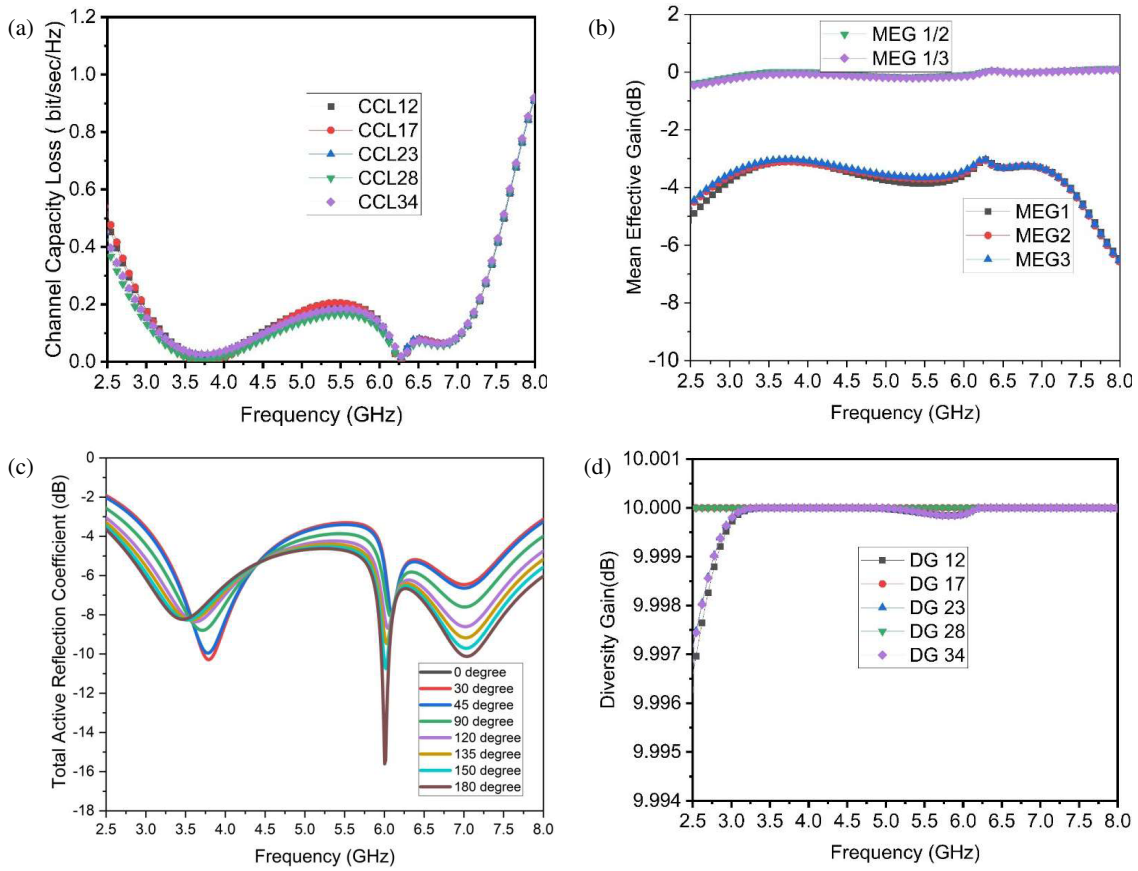

FIGURE 11. Suggested design MIMO parameters: (a) CCL, (b) MEG and ratio of MEG, (c) TARC, (d) Diversity gain.

The total active reflection coefficient (TARC) is another important metric, which quantifies the relationship between emitted and received power [18]. The ideal total active reflection coefficient (TARC) for a MIMO antenna is 0 dB. Figure 11(c) presents TARC values of the suggested antenna, after exciting one port at $1e^{j0}$ when all other ports have the same amplitude with varying excitation phases.

$$\begin{aligned} \sigma_{ii} &= 1 - \left(|T_{ii}|^2 - |T_{ij}|^2\right) \\ \sigma_{ij} &= -\left(T_{ii}^* T_{ij} + T_{ji} T_{jj}^*\right) \end{aligned} \tag{4}$$

Here, both σ_{ij} and σ_{ii} are numbered as Equation (4).

With each different phase excitation, the proposed antenna is affected slightly. Total reflection of antennas is represented by T_{ii} and T_{jj} at ports i and j, whereas T_{ij} and T_{ji} denote the transmission coefficient between any two ports. In TARC, reflection coefficients for port i and j are represented using S_{ii} and S_{jj} while transmission coefficient between antenna ports is represented via S_{ij} and S_{ji}. TARC is used to identify mismatches or coupling effects among antenna ports by providing phase values. These phase values range from $0°$ to $180°$.

$$TARC = \frac{\sqrt{\left(|(S_{ii} + S_{ij})|^2 + |(S_{ji} + S_{jj})|^2\right)}}{\sqrt{2}} \tag{5}$$

Evaluation formula for diversity gain (DG) [17, 21, 22] is as follows:

$$DG = 10\sqrt{1 - |ECC|^2} \tag{6}$$

The standard DG value required via the MIMO system to function effectively is approximately 10 dB, and that of the suggested MIMO system's DG is illustrated in Figure 11(d), demonstrating excellent antenna diversity performance.

4. COMPARISON WITH EXISTING 5G ANTENNA DESIGNS

Table 1 highlights the advantages of the proposed design, including a wide frequency band that fully encompasses the 5G sub-6 GHz spectrum, compact antenna elements, no ground clearance, excellent isolation, and favorable ECC values.

5. PROPOSED ANTENNA ANALYSIS WITH OTHER COMPONENTS

The incorporation of a MIMO antenna design into a handset, while accounting for other components, such as the dielectric frame and battery, can pose a design challenge. Therefore, it is necessary for the model to include the antenna array while accounting for the other components. The performance of the antenna in the presence of a modelled user hand, battery, and plastic frame is discussed in this section.

TABLE 1. 5G MIMO smartphone antenna comparison with the suggested design.

Ref.	Size[(a)] (mm²)	Metal Rim	P/L Elements	D. L	−6 dB BW (GHz)	Isolation (dB)	η (%)	ECC
Prop.	15 ×7	No	Yes	Yes	3.0–7.5	15	58–78	<0.05
[3]	17 ×6	No	No	Yes	3.3–5.95	15	47–78	<0.11
[5]	21.5 ×6	No	No	No	3.3–5.0	14.5	46–77	<0.1
[6]	21.5 ×5.2	No	No	No	3.2–7.3	12	51–70	<0.07
[7]	12.4 ×7	Yes	Yes	No	3.3–4.3, 4.4–5, 5.15–7.1	11	47–70	<0.09
[8]	15 ×6	Yes	Yes	No	3.3–4.2, 4.4–5, 5.15–5.9	11	40–71	<0.09
[14]	9 ×7	Yes	Yes	No	3.27–5.92	12	50–82	<0.11
[16]	17 ×7	Yes	No	Yes	3.3–6.0	18	40–90	<0.05

Prop.: Proposed, Ref.: Reference, [(a)] = Length ×Height of side rim, BW: Bandwidth, ECC: Envelope Correlation Coefficient, D. L: Decoupling Layout, P\ L elements: Parasitic\ Lumped Elements, η: Efficiency

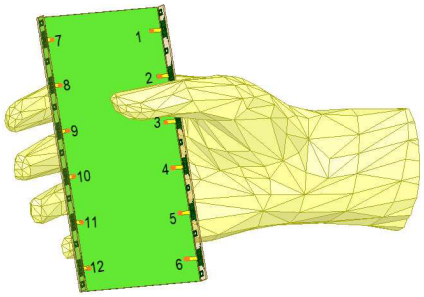

FIGURE 12. Single-hand grip scenario.

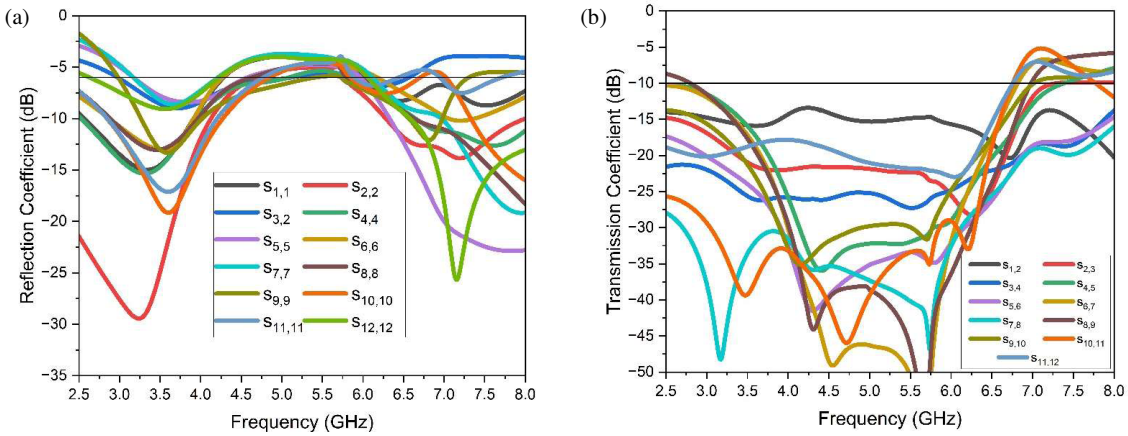

FIGURE 13. S-parameters for single-handed grip scenario: (a) Reflection coefficient, (b) Transmission coefficient.

5.1. User Hand Impact

The human tissue affects the antenna because it is a lossy dielectric with a relative permittivity greater than that of air. The antenna impedance variation and microwave attenuation are the results of the conductivity of the hand, produced by the high-water content. It is important to incorporate hand models to improve antenna design. Figure 12 illustrates the single-handed phone model employed for the user-interaction analysis, whereas Figure 13 presents the corresponding variation in antenna performance under hand-loading conditions. Despite the dielectric loading effects introduced by the user's hand, the proposed antenna successfully maintains its sub-6 GHz impedance bandwidth. Despite these variations, the mutual coupling remained below −10 dB across the operating band, thereby maintaining acceptable isolation performance, as illustrated in Figure 13. This underscores the importance of accounting for hand interactions for an effective antenna design.

5.2. Battery Effect

As shown in Figure 14, a battery element was integrated with the proposed antenna. A metallic block measuring 118 mm×40 mm×3 mm was used to simulate the battery. The battery and ground plane were connected using shorting pins. The results shown in Figure 15 reveal a slight deviation in the

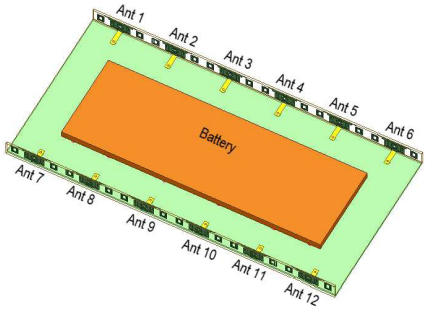

FIGURE 14. Proposed MIMO antenna system with battery.

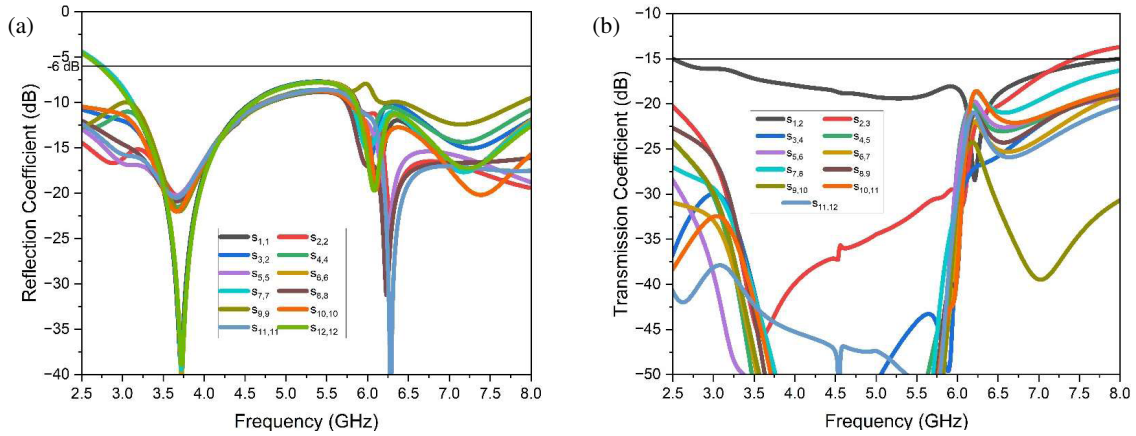

FIGURE 15. S-parameters taking battery effects into account: (a) Coefficients of reflection, (b) Coefficients of transmission.

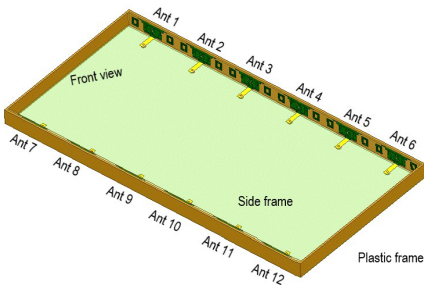

FIGURE 16. Suggested MIMO antenna system with plastic frame.

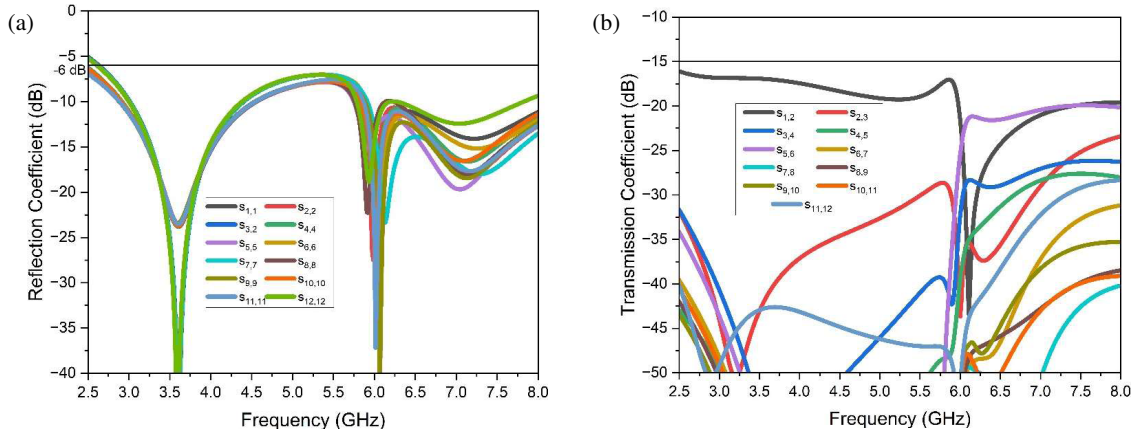

FIGURE 17. S-parameters taking plastic frame into account: (a) Coefficients of reflection, (b) Coefficients of transmission .

resonance frequency. However, the required waveband is still covered by the design, and the isolation remains within the desired limits.

5.3. Effect of the Plastic Frame

As shown in Figure 16, a 7-mm-high plastic frame was mounted around the proposed antenna. Dielectric loading occurs when the plastic frame comes into contact with radiating members owing to their proximity. As shown in Figure 17, the proposed antenna continues to operate within the desired band, with only minor deviations in the S-parameter plots.

6. CONCLUSION

This work presents a 12-element MIMO antenna system that meets the stringent requirements of 5G smartphones by offering ultra-wideband performance, high efficiency, and excellent isolation within a compact footprint. The proposed MIMO antenna exhibits isolation exceeding 15 dB throughout the Sub-6 GHz frequency range (3–7.5 GHz). The proposed structure's other parameters, such as ECC ($<$0.05) and efficiency (58–78%), are obtained by the suggested arrangement and can be considered for future 5G devices, as they address the challenges posed by limited space and mutual coupling, providing a path for more effective antenna designs for modern communication systems.

REFERENCES

[1] Jensen, M. A. and J. W. Wallace, "A review of antennas and propagation for MIMO wireless communications," *IEEE Transactions on Antennas and Propagation*, Vol. 52, No. 11, 2810–2824, 2004.

[2] Agiwal, M., A. Roy, and N. Saxena, "Next generation 5G wireless networks: A comprehensive survey," *IEEE Communications Surveys & Tutorials*, Vol. 18, No. 3, 1617–1655, 2016.

[3] Li, Y., C.-Y.-D. Sim, Y. Luo, and G. Yang, "Multiband 10-antenna array for sub-6 GHz MIMO applications in 5-G smartphones," *IEEE Access*, Vol. 6, 28 041–28 053, 2018.

[4] Hei, Y. Q., J. G. He, and W. T. Li, "Wideband decoupled 8-element MIMO antenna for 5G mobile terminal applications," *IEEE Antennas and Wireless Propagation Letters*, Vol. 20, No. 8, 1448–1452, 2021.

[5] Zhao, A. and Z. Ren, "Wideband MIMO antenna systems based on coupled-loop antenna for 5G N77/N78/N79 applications in mobile terminals," *IEEE Access*, Vol. 7, 93 761–93 771, 2019.

[6] Rai, A. K., R. K. Jaiswal, K. Kumari, K. V. Srivastava, and C.-Y.-D. Sim, "Wideband monopole eight-element MIMO antenna for 5G mobile terminal," *IEEE Access*, Vol. 11, 689–696, 2023.

[7] Cai, Q., Y. Li, X. Zhang, and W. Shen, "Wideband MIMO antenna array covering 3.3–7.1 GHz for 5G metal-rimmed smartphone applications," *IEEE Access*, Vol. 7, 142 070–142 084, 2019.

[8] Zhang, X., Y. Li, W. Wang, and W. Shen, "Ultra-wideband 8-port MIMO antenna array for 5G metal-frame smartphones," *IEEE Access*, Vol. 7, 72 273–72 282, 2019.

[9] Zou, H., Y. Li, C.-Y.-D. Sim, and G. Yang, "Design of 8 × 8 dual-band MIMO antenna array for 5G smartphone applications," *International Journal of RF and Microwave Computer-Aided Engineering*, Vol. 28, No. 9, e21420, 2018.

[10] Wang, H., R. Zhang, Y. Luo, and G. Yang, "Compact eight-element antenna array for triple-band MIMO operation in 5G mobile terminals," *IEEE Access*, Vol. 8, 19 433–19 449, 2020.

[11] Deng, C., D. Liu, and X. Lv, "Tightly arranged four-element MIMO antennas for 5G mobile terminals," *IEEE Transactions on Antennas and Propagation*, Vol. 67, No. 10, 6353–6361, 2019.

[12] Hu, W., L. Qian, S. Gao, L.-H. Wen, Q. Luo, H. Xu, X. Liu, Y. Liu, and W. Wang, "Dual-band eight-element MIMO array using multi-slot decoupling technique for 5G terminals," *IEEE Access*, Vol. 7, 153 910–153 920, 2019.

[13] Chen, Z., Y. Liu, T. Yuan, and H. Wong, "A miniaturized MIMO antenna with dual-band for 5G smartphone application," *IEEE Open Journal of Antennas and Propagation*, Vol. 4, 111–117, 2023.

[14] Chen, H.-D., Y.-C. Tsai, C.-Y.-D. Sim, and C. Kuo, "Broadband eight-antenna array design for sub-6 GHz 5G NR bands metal-frame smartphone applications," *IEEE Antennas and Wireless Propagation Letters*, Vol. 19, No. 7, 1078–1082, 2020.

[15] Sun, L., Y. Li, Z. Zhang, and Z. Feng, "Wideband 5G MIMO antenna with integrated orthogonal-mode dual-antenna pairs for metal-rimmed smartphones," *IEEE Transactions on Antennas and Propagation*, Vol. 68, No. 4, 2494–2503, 2020.

[16] Yuan, X.-T., W. He, K.-D. Hong, C.-Z. Han, Z. Chen, and T. Yuan, "Ultra-wideband MIMO antenna system with high element-isolation for 5G smartphone application," *IEEE Access*, Vol. 8, 56 281–56 289, 2020.

[17] Jaglan, N., S. D. Gupta, and M. S. Sharawi, "18 Element massive MIMO/diversity 5G smartphones antenna design for sub-6 GHz LTE bands 42/43 applications," *IEEE Open Journal of Antennas and Propagation*, Vol. 2, 533–545, 2021.

[18] Shen, L., J. Huang, Q. Li, T. H. Loh, and G. Liu, "Dual-Wideband MIMO antenna with eight elements for 5G and WLAN communication," *Progress In Electromagnetics Research C*, Vol. 144, 65–74, 2024.

[19] Wang, Z., S. Liu, W. Nie, M. Yang, and C. Li, "Broadband eight-element MIMO antenna with high isolation for 5G smartphone applications," *Progress In Electromagnetics Research C*, Vol. 152, 209–219, 2025.

[20] Azim, R., A. K. M. M. H. Meaze, A. Affandi, M. M. Alam, R. Aktar, M. S. Mia, T. Alam, M. Samsuzzaman, and M. T. Islam, "A multi-slotted antenna for LTE/5G Sub-6 GHz wireless communication applications," *International Journal of Microwave and Wireless Technologies*, Vol. 13, No. 5, 486–496, 2021.

[21] Sufian, M. A., N. Hussain, H. Askari, S. G. Park, K. S. Shin, and N. Kim, "Isolation enhancement of a metasurface-based MIMO antenna using slots and shorting pins," *IEEE Access*, Vol. 9, 73 533–73 543, 2021.

[22] Elsharkawy, R. R., A. S. A. El-Hameed, and S. M. El-Nady, "Quad-port MIMO filtenna with high isolation employing BPF with high out-of-band rejection," *IEEE Access*, Vol. 10, 3814–3824, 2021.

[23] Suresh, A. C., C. Althi, O. P. Kumar, M. Alathbah, *et al.*, "Modal analysis-based ultrawideband 4×4 MIMO antenna with flower configuration," *AEU — International Journal of Electronics and Communications*, Vol. 192, 155685, 2025.

[24] Ali, W. A. E. and R. A. Ibrahim, "Highly compact 4×4 flower-shaped MIMO antenna for wideband communications," *Applied Sciences*, Vol. 13, No. 6, 3532, 2023.

[25] Santhakumar, G. and R. Muthukumar, "A novel compact flower shaped antenna array for sub-6 GHZ and UWB applications," *Wireless Networks*, Vol. 31, No. 3, 2925–2938, 2025.

[26] Rahman, M. M., Y. Yang, and S. Dey, "Application of metamaterials in antennas for gain improvement: A study on integration techniques and performance," *IEEE Access*, Vol. 13, 49 489–49 503, 2025.

[27] Singh, V., A. K. Dwivedi, N. K. Narayanaswamy, *et al.*, "Metamaterial/metasurface applications in antenna domain," *Opto-Electronics Review*, e151 692–e151 692, 2024.

[28] Din, I. U., S. Ullah, N. Mufti, R. Ullah, B. Kamal, and R. Ullah, "Metamaterial-based highly isolated MIMO antenna system for 5G smartphone application," *International Journal of Communication Systems*, Vol. 36, No. 3, e5392, 2023.

[29] Fawad, Y., S. Ullah, M. Irfan, R. Ullah, S. Rahman, F. Muhammad, A. H. M. Almawgani, and S. N. F. Mursal, "Dual-polarized 8-port sub 6 GHz 5G MIMO diamond-ring slot antenna for smart phone and portable wireless applications," *PLoS ONE*, Vol. 18, No. 11, e0288793, 2023.